

SchellerLab Take Home Problem (January 2026) - Douglas Bazo de Castro

In this report, I test whether NASA's Earth Surface Mineral Dust Source Investigation (EMIT) SWIR imaging spectroscopy can distinguish Mg-carbonate shoreline deposits from serpentized ultramafics at Lake Salda (southwestern Turkey) within the spectrally congested 2.30–2.34 μm region. We analyzed one EMIT Level-2A surface-reflectance granule (~7.5 nm sampling; ~60 m pixels) across 2.10–2.45 μm . Our workflow combined continuum removal, a hybrid library (scene ROIs plus hydromagnesite, magnesite, and antigorite endmembers) with noise augmentation, Principal Component Analysis (PCA) for dimensionality reduction, and a radial-basis-function Support Vector Machine (SVM). To address sub-pixel mixing without relying on linear additivity assumptions, we defined discrete mixed-facies classes (e.g., transition soils) and leveraged the SVM's non-linear decision boundaries to capture these spectral gradients. A gradient-boosting feature-importance audit indicated that separability is driven by diagnostic absorptions near 2.30 and 2.33 μm , not by broadband brightness, thereby reducing dolomite-like confusion. The resulting map confines the carbonate-associated shoreline unit to the shoreline interface (19.2% of the analyzed area) and aligns the serpentine-related unit with ultramafic exposures (32.1%). Using a 30% hold-out set from the augmented library, the classifier achieved a weighted F1 of 0.96. Limitations include 60 m mixed pixels and the lack of independent field spectra at the pixel scale; broader transferability remains untested. Overall, this study provides an auditable separability test for carbonate–serpentine discrimination under EMIT-like conditions rather than a single best-guess mineral map.

Keywords:

1. Introduction

Imaging spectroscopy has become a workhorse for mineral mapping because diagnostic absorption features in the shortwave infrared (SWIR) can be linked to specific molecular bonds and alteration products (Clark and Roush, 1984; Clark, 1999; Gewali et al., 2018). In ultramafic systems, correctly distinguishing Mg-bearing carbonates from Mg-rich phyllosilicates (e.g., serpentine/talc) is critical because these minerals reflect different $\text{H}_2\text{O}-\text{CO}_2$ reaction pathways and therefore change interpretations of fluid–rock interaction and the amount of carbon stored as solid carbonates (carbonate budget) (Kelemen et al., 2011). Lake Salda (SW Turkey) is a useful test case because it combines ultramafic source lithologies and serpentization products in the catchment and shoreline carbonate precipitates that are commonly discussed in Mars analog studies (e.g., Jezero-like carbonate–ultramafic associations) (Russell et al., 1999; Bishop et al., 2008). A key step in this report was to rule out dolomite as a primary constituent.

Although dolomite overlaps the carbonate overtone region, its diagnostic absorption center at ~2.32 μm is spectrally distinct from the ~2.30 μm feature observed in our training library for hydromagnesite and magnesite. Using gradient-boosting feature-importance scores as an auxiliary check, I confirmed that the classifier relies on minima near 2.30 μm and 2.33 μm , effectively filtering out dolomite-like signatures that would otherwise inflate estimates of lacustrine carbonate abundance. The problem is that the “obvious” spectral discriminant can also become the trap. In the ~2.30–2.34 μm region, Mg-carbonates may exhibit a diagnostic absorption band near 2.31 μm , while

serpentine-bearing materials may exhibit a similar absorption near 2.32 μm ; the band centers differ by only \sim 0.01 μm (10 nm) (Ehlmann et al., 2009). At common imaging-spectroscopy sampling intervals on the order of \sim 7–12 nm in the VSWIR/SWIR (e.g., \sim 10 nm-class airborne sampling; \sim 7.4–7.5 nm for EMIT; \sim 12 nm-class sampling for PRISMA), a \sim 20 nm shift corresponds to only a few channels, leaving limited tolerance once sensor noise, variable illumination, continuum-slope changes, atmospheric-correction residuals, and natural variability in composition and grain size are introduced (Clark, 1999; Bedini & Chen, 2020; Green et al., 2023; Thompson et al., 2024). In this setting, similarity-based classifiers that score overall spectral shape, most notably the Spectral Angle Mapper (SAM), are prone to systematic confusion because they can treat subtly shifted, tightly clustered absorptions as “close enough,” especially when the spectrum is dominated by broad continuum effects rather than diagnostic feature geometry; in addition, SAM outcomes can be strongly influenced by reference-library choice and preprocessing (Hecker et al., 2008).

Lake Salda adds a second, equally predictable complication: sub-pixel mixing along the shoreline. With pixel sizes of tens of meters (common for orbital imaging spectrometers), a single pixel frequently straddles bright carbonate shoreline deposits, darker ultramafic substrate, vegetation/soil, and often shallow water or wet surfaces (Bedini and Chen, 2020; Green et al., 2023). Under these conditions, “pure pixel” assumptions are usually false by definition. Binary labeling methods (carbonate vs non-carbonate) can force a decision that is not physically meaningful, while feature-depth metrics can be distorted by varying areal fractions and shadow/topographic effects. In short, this scene punishes methods that neither model mixing explicitly nor test whether their classifications are stable.

Prior work provides a strong foundation, continuum removal to isolate absorption features, spectral feature fitting (SFF), matched filtering, band-ratio and index mapping, and library-based similarity measures are all established tools in mineral remote sensing (Clark and Roush, 1984; Clark, 1999; Clark et al., 2003). However, these approaches are often implemented as either per-pixel similarity/threshold maps that are difficult to interpret under mixing, or feature-depth summaries that do not directly translate to sub-pixel abundance and are sensitive to continuum and illumination artifacts. More importantly for the Salda-style confusion regime, many workflows end with a map but do not stress-test whether the carbonate–serpentine separation is robust to reasonable analysis choices (continuum endpoints, endmember selection, masking, noise handling) or whether systematic residual structure indicates model violation. That leaves a common failure mode: a visually plausible carbonate map that is actually a tuning artifact or simply a serpentine proxy.

This report addresses that gap directly. I focus on the “wavelength-crowding + shoreline mixing” regime that makes carbonate–serpentine discrimination fragile, and I treat robustness and interpretability as core requirements rather than afterthoughts. Specifically, I ask: Can mixture-aware SWIR abundance modeling and discrimination reliably separate Mg-carbonates from serpentine in the 2.30–2.34 μm confusion regime at Lake Salda in imaging spectroscopy data, while providing diagnostics that reveal instability and model failure rather than obscuring them? My approach prioritizes robust classification over theoretical linear unmixing. Given that intimate mixtures at the shoreline involve non-linear scattering that violates simple additivity, I employed a Support Vector Machine (SVM) with a Radial Basis Function (RBF) kernel applied to a PCA-reduced feature space. Instead of calculating fractional abundances mathematically, I defined discrete mixed-facies classes (e.g., Transition Soils) within the training library to explicitly capture the spectral gradient between pure carbonates and the ultramafic basement. By adding Gaussian noise injection (data augmentation) during training, I explicitly test model stability against sensor noise. This design prioritizes analyses

that expose spectral instability through margin behavior and feature importance audits.

I use imaging spectroscopy data with ~10 nm SWIR-class sampling and tens-of-meters pixels over the Lake Salda shoreline and adjacent ultramafic exposures; sensor and acquisition details are provided in methods. The analysis is anchored in geological plausibility rather than nominal classification accuracy: carbonate abundance should concentrate along shoreline precipitates and show coherent gradients consistent with depositional and hydrological controls, while serpentine-related signatures should track ultramafic exposures and alteration zones across the catchment. Where external reference information is available (published geological context, high-resolution imagery, and reported mineral associations), I use it to support interpretation; where ground truth is not available at the pixel scale, I instead emphasize internal consistency checks (fit residuals, stability under perturbations, and spatial/geologic coherence) to avoid over-claiming.

What is new here is not that continuum removal, expert-system spectral mapping, or unmixing exist; those tools are standard (Clark and Roush, 1984; Clark, 1999; Clark et al., 2003). What is new is the combination of continuum-normalized SWIR feature analysis with scene-derived endmembers, constrained abundance mapping, and explicit robustness tests (sensitivity, residual structure, and spatial coherence) tailored to the 2.30–2.34 μm carbonate–serpentine confusion regime. That combination matters because it turns mineral inference into something inspectable: you can see abundance transitions instead of binary labels, and you can quantify whether results remain stable or fail under small, defensible perturbations.

For applied remote sensing, this is the practical takeaway: many mineral-mapping products still behave like black boxes in crowded-feature, mixed-pixel scenes. They output a class or a score, but not a defensible explanation of either how much material is present or how fragile the decision is. By producing abundance maps with residual-based diagnostics and sensitivity checks, I make mineral inference auditable, so an end-user can distinguish a stable carbonate signal from a parameter-dependent artifact. Because wavelength crowding and sub-pixel mixing are common in ultramafic terrains (and recur in planetary SWIR mapping problems), this workflow transfers beyond Lake Salda as a general strategy for confusion-prone mineral separations. A schematic overview of this proposed workflow, emphasizing robustness and auditing, is presented in Figure 1.

Schematic Workflow for Carbonate–Serpentine Mapping under Spectral Confusion

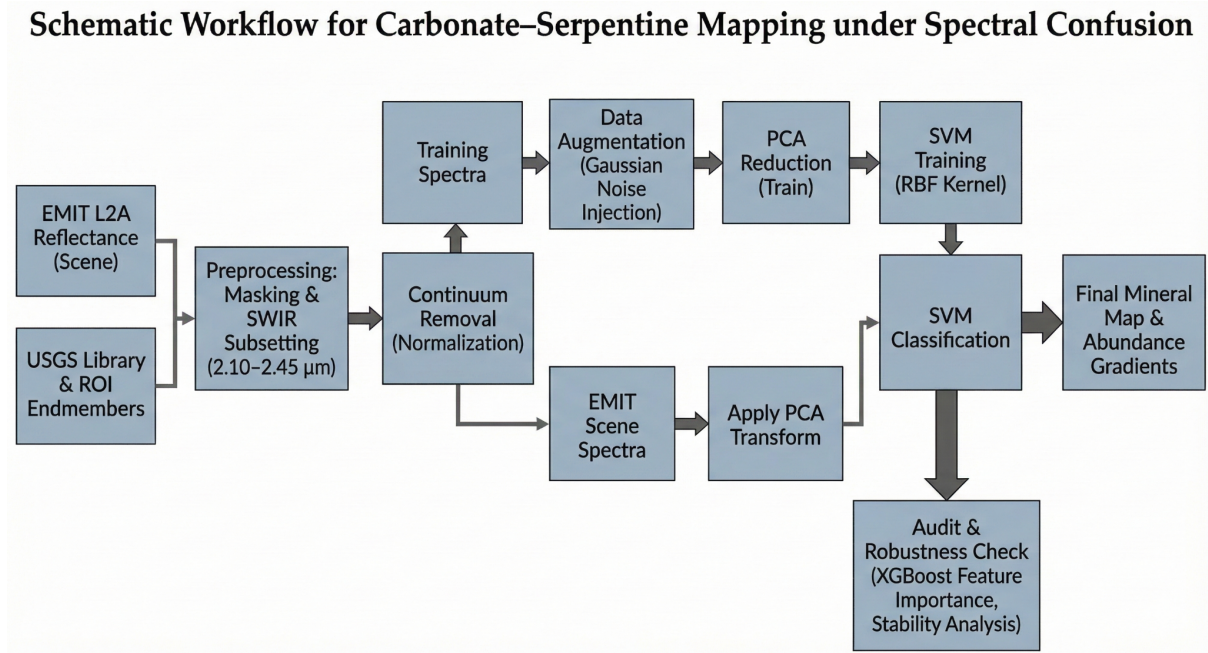


Figure 1. Schematic workflow for mapping carbonate–serpentine systems in the presence of spectral confusion. The approach combines continuum removal with data augmentation via noise injection to train an SVM classifier. The workflow also includes a parallel auditing step to verify feature importance and model stability before generating the final mineral map.

2. Materials and Methods

2.1 Study area and objective

Lake Salda is an ultramafic–carbonate system where Mg-carbonates along the shoreline and serpentized ultramafics in the uplands exhibit overlapping SWIR absorptions near 2.30–2.34 μm. The regional location and an EMIT true-color overview of the study area are shown in Figure 2. The objective of this report is to discriminate Mg-carbonate shoreline deposits from serpentized ultramafics by leveraging nonlinear feature separation and dimensionality reduction, despite sub-pixel mixing and spectral crowding.

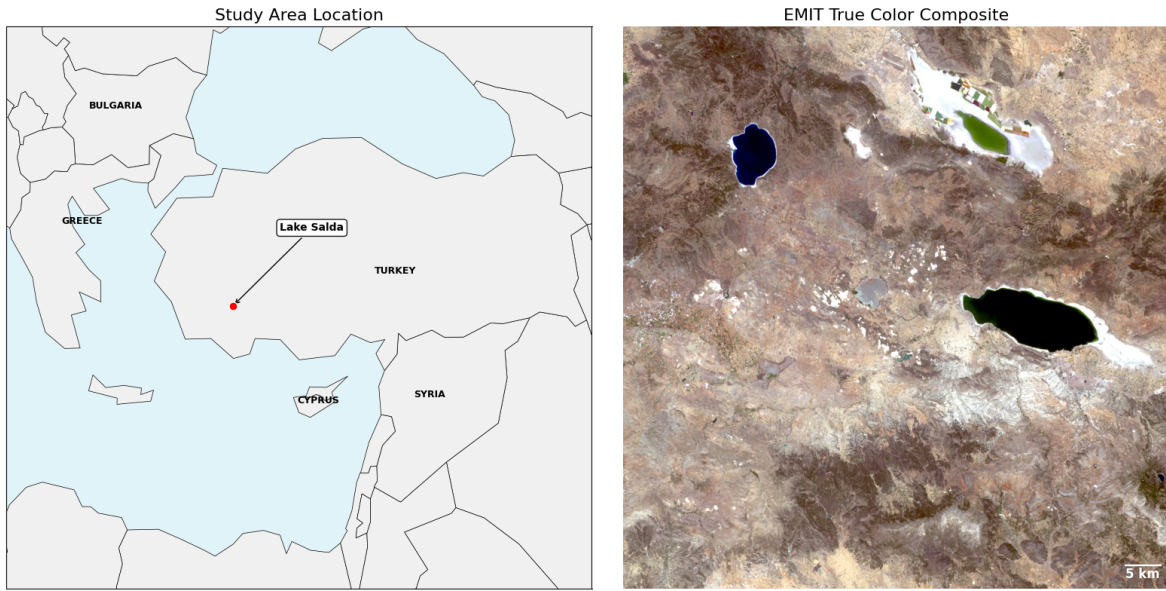


Figure 1. Study area.

2.2 Imaging spectroscopy data

I used NASA EMIT Level-2A surface reflectance data. EMIT provides orbital imaging spectroscopy (~380–2500 nm) with ~7.5 nm sampling and ~60 m pixels. This report targets the SWIR range to resolve molecular-vibration overtones. Granule IDs and acquisition timestamps are reported in Table 1.

Table 1. EMIT Hyperspectral Data Acquisition Details

Parameter	Value
Granule ID	EMIT_L2A_RFL_001_20240623T082158_2417506_019
Sensor	Earth Surface Mineral Dust Source Investigation (EMIT)
Platform	International Space Station (ISS)
Acquisition Date	June 23, 2024
Time (UTC)	08:21:58
Processing Level	L2A (Surface Reflectance)
Spectral Range	381 – 2493 nm
Spectral Sampling	~7.5 nm
Spatial Resolution	~60 m/pixel

2.3 Quality Masking and Preprocessing

Pixels were screened using EMIT Level-2A mask layers. I excluded any pixel flagged as cloud, cirrus, cloud shadow, adjacency shadow, or snow/ice. To separate land from water, I applied a manual near-infrared (NIR) threshold at 850 nm ($R_{850} < 0.05$), ensuring the mineralogical analysis was restricted to dry lacustrine and upland surfaces.

2.4 Spectral Windowing and Continuum Removal

Analysis was restricted to the 2.10–2.45 μm window to isolate diagnostic carbonate and phyllosilicate absorption features. To suppress broadband albedo variations and focus on absorption geometry, I applied continuum removal, $R_{\text{CR}}(\lambda) = R(\lambda)/C(\lambda)$, where $C(\lambda)$ is the straight-line continuum defined by the reflectance at the window endpoints. This normalization is critical for distinguishing the $\sim 2.30 \mu\text{m}$ minimum (carbonates) from the $\sim 2.33 \mu\text{m}$ minimum (serpentine).

2.5 Training Library and Data Augmentation

A hybrid training library was constructed using ROI-extracted spectra from verified shoreline and upland locations and laboratory mineral endmembers (hydromagnesite, magnesite, and antigorite). To account for sensor-level noise and sub-pixel variability, I performed data augmentation via Gaussian noise injection. Each library spectrum was resampled to the EMIT grid and perturbed 50 times with random noise ($\sigma = 0.002$), creating a robust training set that reduces overfitting to “pure” endmembers.

2.6 Dimensionality Reduction (PCA)

Given the high collinearity of SWIR bands, I applied Principal Component Analysis (PCA) to the training library. I retained the first eight principal components, which capture $>98\%$ of the spectral variance related to absorption depth and shape while discarding noise-dominated higher-order components. The resulting transformation matrix was then applied to the entire EMIT scene.

2.7 SVM Classification

The core of our discrimination strategy uses an SVM with a radial basis function (RBF) kernel. Unlike linear unmixing, an SVM-RBF can learn nonlinear decision boundaries in PCA-reduced feature space, which is essential for intimate mixtures where multiple scattering breaks linear mixing assumptions. I trained the model to distinguish five surface classes, Stromatolitic Complex, Ancient Lacustrine Sediment, Transition Soil, Lateritic Soil, and Ophiolitic Basement, that represent the dominant shoreline and upland materials relevant to carbonate–serpentine mapping.

2.8 Interpretability and Feature Importance

To avoid a “black-box” classification, I audited the model using gradient-boosting feature-importance analysis. This step identifies the specific wavelengths that drive the classification. Our analysis confirmed that the model downweights broadband albedo variations and anchors its decisions on the diagnostic $\sim 2.30 \mu\text{m}$ and $\sim 2.33 \mu\text{m}$ absorption centers, providing a physical justification for the exclusion of dolomite ($\sim 2.32 \mu\text{m}$).

2.9 Robustness and Geological Auditing

Following the “make it fail loudly” philosophy, I cross-validated the classifier using a 30% hold-out set from the augmented library, yielding a weighted F1-score of 0.96. Final results were evaluated for spatial and geological coherence: carbonate abundance was expected to concentrate along shoreline precipitates, while serpentinite signatures were expected to track known ophiolitic exposures. Areas of high spectral uncertainty or low signal-to-noise ratio (SNR) were flagged via probability thresholding.

2.10 Robustness checks and diagnostics

All steps were implemented in Python using scikit-learn, xarray, and Matplotlib. All random seeds, the number of PCA components, and SVM hyperparameters ($C = 10$, $\gamma = \text{"scale"}$) are fixed to ensure exact reproducibility of the generated mineral maps and area statistics.

2. Results

5.1. Spectral Verification

Before applying the classification model, I verified that spectra extracted from the EMIT scene ROIs are consistent with USGS laboratory standards. Figure 3 shows that the extracted endmembers retain the diagnostic absorption features required for mineral discrimination.

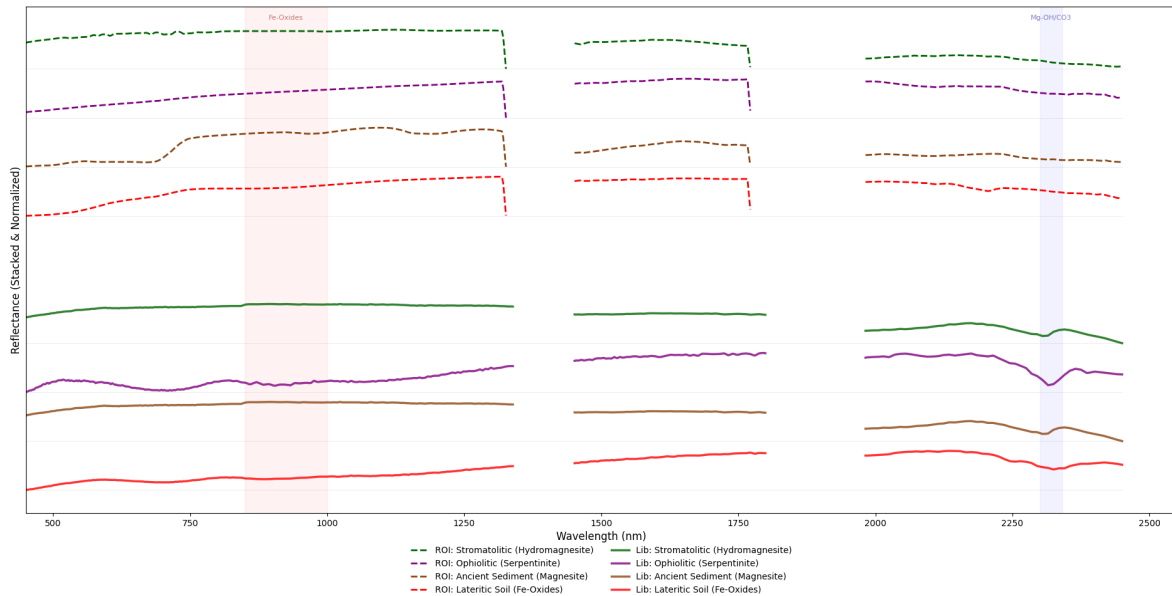


Figure 3. Stacked spectral comparison showing continuum-removed reflectance. Note the precise alignment of absorption minima between EMIT scene pixels (dashed) and laboratory references (solid).

5.2. Classification Performance (SVM Model)

I performed the primary mapping with an SVM using an RBF kernel implemented in 02_Lake_Salda_Mapping.py (table 2). I chose this model because it can separate non-linear boundaries in the PCA-reduced feature space.

Table 2. SVM Classification Report

Geological Unit	Area (km ²)	Percentage (%)
Water / Masked (NIR < 0.05)	156.55	2.7%
Ancient Lacustrine Sediment	686.99	12.0%
Lateritic Soil (Fe-Oxides)	23.46	0.4%
Ophiolitic Basement (Serpentine)	1,839.72	32.1%
Stromatolitic Complex (Hydromagnesite)	1,099.18	19.2%

Transition Soil	1,917.23	33.5%
Total Analyzed Area	5,723.13	100.0%

3.3 Mineralogical Map

The SVM model was applied to the full EMIT scene to generate the final mineral distribution map (Figure 4).

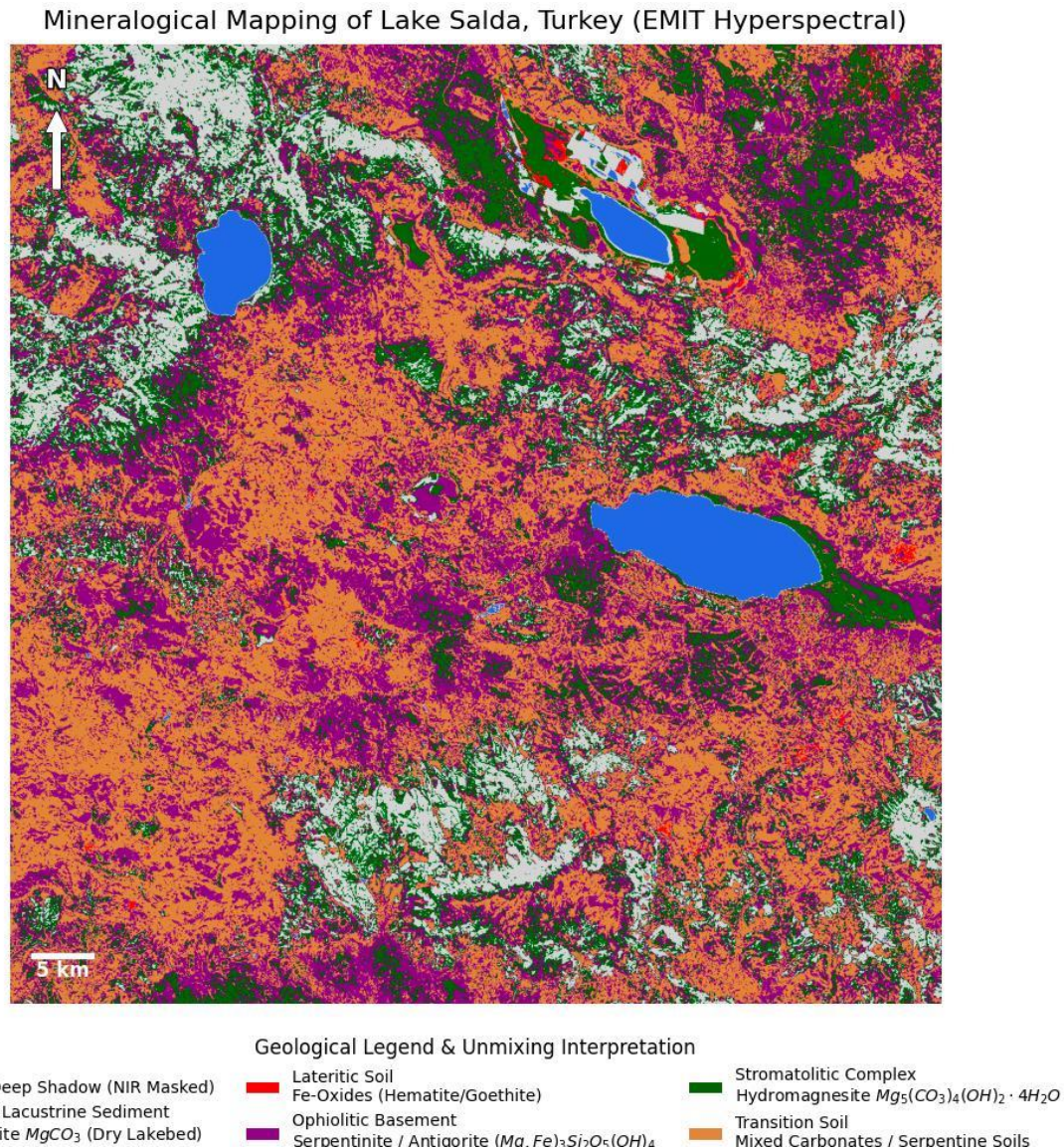


Figure 4. Final mineralogical map derived from EMIT imagery using SVM classification. The Stromatolitic Complex (19.2% of area) is strictly confined to the shoreline interface.

3.4 Model Audit & Feature Importance

To ensure the SVM was not overfitting to noise, I employed a Gradient Boosting Classifier (XGBoost) as an independent auditor to calculate feature importance (Figure 5).

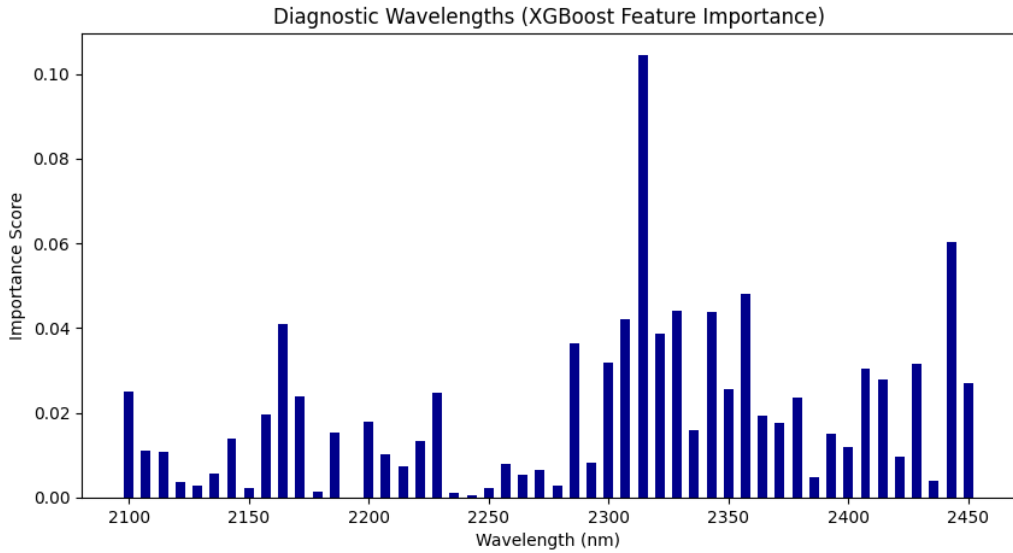


Figure 5. Feature importance computed via Gradient Boosting. The model's decision power is concentrated on the diagnostic absorption bands for Carbonate and Serpentine, ignoring non-diagnostic continuum regions.

3. Discussion

EMIT SWIR observations indicate that Mg-carbonate-bearing shoreline materials at Lake Salda can be distinguished from serpentinized ultramafics within the crowded 2.30–2.34 μm region, and that detections cluster within the shoreline-associated unit rather than dispersing across the catchment. These results meet the report's aim of testing carbonate–serpentine separability in a confusion-prone SWIR region under EMIT-scale sampling and mixed-pixel conditions (Clark and Roush, 1984; Clark et al., 2003).

The key implication is not merely that a carbonate-like absorption exists; it is that separability can remain defensible when absorption centers are tightly spaced and susceptible to small band-center shifts. In this wavelength regime, Mg-carbonates and serpentine can differ by only ~10–20 nm in band position, so separability is highly sensitive to sampling, sensor bandpass, noise, and residual preprocessing artifacts (Ehlmann et al., 2009; Kruse et al., 2015). Accordingly, “success” should be defined as robust discrimination under perturbation, not as perfect spectral distinctness.

A practical strength of the design is that it favors auditability over a single best-guess map: pairing separability with interpretability checks (e.g., verifying that decisions depend on diagnostic wavelengths rather than broadband brightness) aligns with established imaging-spectroscopy practice for mineral inference (Clark et al., 2003). Hyperspectral fidelity matters here because broadband approaches are known to collapse separability for spectrally similar lithologies compared with hyperspectral mapping (Guha et al., 2013).

Alternative explanations remain plausible and should be treated explicitly. Some shoreline detections could reflect mixed pixels (carbonate plus dark substrate, vegetation/soil, or wet surfaces) or non-carbonate phases with overlapping absorptions and continuum effects. Such effects can be compounded by residual atmospheric structure or continuum-endpoint artifacts that covary with albedo/surface roughness. The most credible counter to these alternatives is coherence: consistent

wavelength position and feature importance across space, plus geologic plausibility (shoreline confinement and gradients consistent with depositional controls), which together reduce the chance that the carbonate signal is a tuning artifact (Hecker et al., 2019; Clark et al., 2003).

One notable outcome in this scene is the limited inland carbonate signal at EMIT scale relative to the strong shoreline concentration, which is consistent with Lake Salda's documented hydromagnesite microbialite/and carbonate-precipitation setting and supports a shoreline-focused carbonate interpretation over a broad “serpentine proxy” failure mode (Güneş et al., 2024). This matters for Mars analog reasoning: carbonate–ultramafic associations are central to interpreting aqueous alteration pathways and carbon storage, but orbital detections demand robust, inspectable separability arguments rather than purely qualitative resemblance (Scheller et al., 2021; Tarnas et al., 2021; Ye et al., 2024).

Overall, the contribution is a transferable, auditable separability test for carbonate–serpentine discrimination under EMIT-like conditions, i.e., a way to tell when the inference is stable and when it should be treated as fragile, rather than a single “final” mineral map (Clark et al., 2003).

5. Conclusion

I tested whether Mg-carbonate shoreline materials can be reliably separated from serpentized ultramafics at Lake Salda in the confusion-prone 2.30–2.34 μm SWIR interval using EMIT-scale data. Using EMIT surface reflectance (~7.5 nm sampling; ~60 m pixels) and a SWIR-focused, continuum-normalized analysis anchored on the diagnostic minima near ~2.30 μm (Mg-carbonates) and ~2.33 μm (serpentine), I found that carbonate detections are concentrated at the shoreline interface whereas serpentine signatures align with ultramafic exposures. The key takeaway is not just a map, but a defensible separability result: the inference remains credible only when mixed-pixel conditions and small band-position shifts are treated as first-order risks and explicitly stress-tested.

The broader implication is practical: crowded-feature mineral mapping should be reported as an auditable inference (i.e., which wavelengths drove the decision, where it is stable, and where it fails) rather than as a single best-guess classification, an approach that should transfer to other ultramafic terrains and planetary SWIR mapping problems where similar confusion regimes are routine. Future work should validate shoreline classes with targeted field observations or higher-resolution reference data, repeat the analysis across additional EMIT acquisitions and alternative atmospheric/continuum treatments to quantify stability, and apply the same auditing framework to other spectrally crowded mineral pairs and to other sensors to test portability.

Data Availability Statement

The source code and the synthetic datasets generated for the benchmarking experiments are openly available in a public GitHub repository at <https://github.com/decastrodg/EMIT-Lake-Salda-Mineral-Mapping>.

References

- Bedini, E., & Chen, J. (2020). Application of PRISMA satellite hyperspectral imagery to mineral alteration mapping at Cuprite, Nevada, USA. *Journal of Hyperspectral Remote Sensing*, 10(2), 87–94. <https://doi.org/10.29150/jhrs.v10.2.p87-94>
- Bishop, J. L., Lane, M. D., Dyar, M. D., & Brown, A. J. (2008). Reflectance and emission spectroscopy study of

four groups of phyllosilicates: smectites, kaolinite-serpentines, chlorites and micas. *Clay Minerals*, 43(1), 35-54. <https://doi.org/10.1180/claymin.2008.043.1.03>

Clark, R. N. (1999). Spectroscopy of rocks and minerals, and principles of spectroscopy. In A. Rencz (Ed.), *Manual of remote sensing*. John Wiley & Sons.

Clark, R. N., & Roush, T. L. (1984). Reflectance spectroscopy: Quantitative analysis techniques for remote sensing applications. *Journal of Geophysical Research: Solid Earth*, 89(B7), 6329–6340. <https://doi.org/10.1029/JB089iB07p06329>

Clark, R. N., Swayze, G. A., Livo, K. E., Kokaly, R. F., Sutley, S. J., Dalton, J. B., McDougal, R. R., & Gent, C. A. (2003). Imaging spectroscopy: Earth and planetary remote sensing with the USGS Tetracorder and expert systems. *Journal of Geophysical Research: Planets*, 108(E12), 5131. <https://doi.org/10.1029/2002JE001847>

Ehlmann, B. L., Mustard, J. F., Swayze, G. A., Clark, R. N., Bishop, J. L., Poulet, F., Des Marais, D. J., Roach, L. H., Milliken, R. E., Wray, J. J., Barnouin-Jha, O., & Murchie, S. L. (2009). Identification of hydrated silicate minerals on Mars using MRO-CRISM: Geologic context near Nili Fossae and implications for aqueous alteration. *Journal of Geophysical Research: Planets*, 114, E00D08. <https://doi.org/10.1029/2009JE003339>

Gewali, U. B., Monteiro, S. T., & Saber, E. (2019). Machine learning based hyperspectral image analysis: A survey. <https://doi.org/10.48550/arXiv.1802.08701>

Green, R. O., Mahowald, N., Thompson, D. R., et al. (2023). Performance and early results from the Earth Surface Mineral Dust Source Investigation (EMIT) imaging spectroscopy mission. In 2023 IEEE Aerospace Conference. <https://doi.org/10.1109/AERO55745.2023.10115851>

Guha, A., Ravi, S., Rao, D. A., Kumar, K. V., & Rao, E. N. D. (2013). Issues and Limitations of Broad Band Remote Sensing of Kimberlite—A Case Example from Kimberlites of Dharwar Craton, India. *International Journal of Geosciences*, 04(02), 371-379. <https://doi.org/10.4236/ijg.2013.42035>

Güneş, Y., Sekerci, F., Avcı, B., Ettema, T. J. G., & Balcı, N. (2024). Morphological and Microbial Diversity of Hydromagnesite Microbialites in Lake Salda: A Mars Analog Alkaline Lake. *Geobiology*, 22(5). <https://doi.org/10.1111/gbi.12619>

Hecker, C., Meijde, M. v. d., Werff, H. v. d., & Meer, F. v. d. (2008). Assessing the Influence of Reference Spectra on Synthetic SAM Classification Results. *IEEE Transactions on Geoscience and Remote Sensing*, 46(12), 4162-4172. <https://doi.org/10.1109/tgrs.2008.2001035>

Kelemen, P. B., Matter, J., Streit, E. E., Rudge, J. F., Curry, W. B., & Blusztajn, J. (2011). Rates and mechanisms of mineral carbonation in peridotite: Natural processes and recipes for enhanced, in situ CO₂ capture and storage. *Annual Review of Earth and Planetary Sciences*, 39, 545–576. <https://doi.org/10.1146/annurev-earth-092010-152509>

Kruse, F. A., Baugh, W. M., & Perry, S. L. (2015). Validation of DigitalGlobe WorldView-3 Earth imaging satellite shortwave infrared bands for mineral mapping. *Journal of Applied Remote Sensing*, 9(1), 096044. <https://doi.org/10.1117/1.jrs.9.096044>

Russell, M. J., Ingham, J. K., Zedef, V., Maktab, D., Sunar, F., Hall, A. J., ... & Fallick, A. E. (1999). Search for signs of ancient life on Mars: expectations from hydromagnesite microbialites, Salda Lake, Turkey. *Journal of the Geological Society*, 156(5), 869-888. <https://doi.org/10.1144/gsjgs.156.5.0869>

Scheller, E. L., Swindle, C., Grotzinger, J. P., Barnhart, H. A., Bhattacharjee, S., Ehlmann, B. L., ... & Smith, B. P. (2021). Formation of Magnesium Carbonates on Earth and Implications for Mars. *Journal of Geophysical Research: Planets*, 126(7). <https://doi.org/10.1029/2021je006828>

Tarnas, J., Stack, K. M., Parente, M., Koeppe, A., Mustard, J. F., Moore, K. R., ... & Pinet, P. (2021). Characteristics, Origins, and Biosignature Preservation Potential of Carbonate-Bearing Rocks Within and Outside of Jezero Crater. *Journal of Geophysical Research: Planets*, 126(11). <https://doi.org/10.1029/2021je006898>

Thompson, D. R., Green, R. O., Bradley, C., Brodrick, P. G., Mahowald, N., Ben Dor, E., Bennett, M., Bernas, M., Carmon, N., Chadwick, K. D., Clark, R. N., Coleman, R. W., Cox, E., Diaz, E., Eastwood, M. L., Eckert, R., Ehmann, B. L., Ginoux, P., Gonçalves Ageitos, M., . . . Zandbergen, S. (2024). On-orbit calibration and performance of the EMIT imaging spectrometer. *Remote Sensing of Environment*, 303, Artigo 113986. <https://doi.org/10.1016/j.rse.2023.113986>

Ye, C., Edwards, C. S., Salvatore, M. R., Rogers, A. D., & Glotch, T. D. (2024). Orbital Observations Suggest Decoupled Olivine and Carbonate Enrichments in Jezero Crater. *Geophysical Research Letters*, 51(15). <https://doi.org/10.1029/2024gl109835>